ChemSusChem

Research Article
doi.org/10.1002/cssc.202201046

Chemistry Europe
European Chemical Societies Publishing

www.chemsuschem.org

Eco-Friendly Synthesis of 3D Disordered Carbon Materials for High-Performance Dual Carbon Na-Ion Capacitors

Alba Fombona-Pascual,[a] Noel Díez,[a] Antonio B. Fuertes,[a] and Marta Sevilla*[a]

An eco-friendly and sustainable salt-templating approach was proposed for the production of anode materials with a 3D sponge-like structure for sodium-ion capacitors using gluconic acid as carbon precursor and sodium carbonate as water-removable template. The optimized carbon material combined porous thin walls that provided short diffusional paths, a highly disordered microstructure with dilated interlayer spacing, and a large oxygen content, all of which facilitated Na ion transport and provided plenty of active sites for Na adsorption. This material provided a capacity of 314 mAh g^{-1} at 0.1 A g^{-1} and 130 mAh g^{-1} at 10 A g^{-1}. When combined with a 3D highly porous carbon cathode (S_{BET} ≈2300 $m^2 g^{-1}$) synthesized from the same precursor, the Na-ion capacitor showed high specific energy/power, that is 110 Wh kg^{-1} at low power and still 71 Wh kg^{-1} at approximately 26 kW kg^{-1}, and a good capacity retention of 70% over 10000 cycles.

Introduction

Hybrid ion capacitors (HICs), integrating a battery-type negative electrode (anode) and a capacitor-type positive electrode (cathode), have emerged as a viable solution to the shortcomings of other devices: energy storage limitations of supercapacitors and low power and short cyclability of batteries. In other words, they can bridge the performance gap between Li/Na-ion batteries and supercapacitors, meeting the growing demands for electric automotive and regenerative energy storage applications.

In particular, Na-ion capacitors (NICs) are attracting much attention due to the abundance of sodium sources compared to lithium ones, their more even geographical distribution and their lower cost. Besides, Na does not react with aluminum, so that this metal is suitable as current collector instead of the expensive copper required for lithium-based systems. The charge storage mechanism of these devices is based on the reversible anion adsorption/desorption on the surface of the cathode and Na-ion reversible intercalation/de-intercalation in the anode. Currently, the main bottleneck in the development of these devices is the design and synthesis of high-performance anodes which combine a high capacity with high sodiation/de-sodiation rates to match the fast ion adsorption process over the cathode. Among the variety of candidate materials, carbon materials are very attractive due to their high chemical and electrochemical stability, good conductivity, potential low cost and easily tunable chemical and physical properties. Graphite, widely used as anode in Li-ion batteries, cannot be used in the Na-counterparts due to the instability of the sodium intercalation compounds in carbonate-based electrolytes.[1] In contrast, highly disordered carbons such as hard carbons have shown their potential in Na-ion batteries, with capacities already exceeding in some cases 300 mAh g^{-1}.[2–5] However, their Na storage kinetics is too slow for their implementation in Na-ion capacitors on account of their predominantly diffusion-controlled sodium storage mechanism, that is intercalation/de-intercalation. Carbon materials targeted at NICs should promote the fast pseudocapacitive sodium storage mechanism in the sloping region at high potentials (>0.1 V vs. Na/Na^+), as well as provide shortened diffusion distances to speed up sodium ions transport. With that aim, nanostructure design and heteroatom doping have been commonly examined. Thus, doping with heteroatoms such as nitrogen, sulfur, oxygen or phosphorus introduces additional actives sites for the reversible binding of polar Na^+ cations through fast pseudocapacitive processes, creates additional defects for Na^+ adsorption, increases the interlayer distance, and enhances the electronic conductivity and wettability. These improvements have led to capacities well above 300 mAh g^{-1} at low rates, while still preserving capacities above 100 mAh g^{-1} at high rates (>5 A g^{-1}).[6–10] On the other hand, the use of 1D, 2D and 3D nanostructures has brought about significant improvements in the performance at high rates on account of improved ion transport and electron conduction.[11–13] However, in many cases, such materials are produced by adopting complicated synthesis processes or non-sustainable carbon resources (e.g., pitch).[14–16] From a scaling up point of view, the use of biomass-based products as carbon precursors in combination with easy, efficient and green synthesis processes is highly desirable. In this regard, the environmentally-sound salt-templating technique can easily modulate the morphology of carbons prepared from certain biomass-derived compounds, leading to high-performance supercapacitor electrodes and Na-ion battery anodes.[17–22]

[a] A. Fombona-Pascual, Dr. N. Díez, Prof. A. B. Fuertes, Dr. M. Sevilla
Instituto de Ciencia y Tecnología del Carbono (INCAR), CSIC
Francisco Pintado Fe 26, 33011 Oviedo (Spain)
E-mail: martasev@incar.csic.es

Supporting information for this article is available on the WWW under https://doi.org/10.1002/cssc.202201046

Herein, we adopt a salt-templating approach to produce 3D sponge-like carbons from gluconic acid (GA), which is a natural product arising from the oxidation of glucose, and is characterized by a relatively high yield and low melting temperature. A low-cost, low toxicity and water-removable salt such as sodium carbonate is selected as salt template. The carbon materials thus produced show a predominant pseudocapacitive sodium storage mechanism and the optimized material provides a capacity of 314 mAh g^{-1} at 0.1 A g^{-1} and still 130 mAh g^{-1} at 10 A g^{-1}. A 3D highly porous carbon (S_{BET} ≈2300 g^{-1}) is synthesized from the same precursor following a salt template-assisted chemical activation strategy based on the use of K_2CO_3 and KCl, which was developed by our group.[23,24] The Na-ion capacitor assembled with such anode and cathode materials is able to combine a high specific energy/power (up to 110 Wh kg^{-1} and 26 kW kg^{-1} respectively) with a capacity retention as high as 70% over 10000 cycles.

Results and Discussion

Structural and chemical properties of the anode carbon materials

Scheme 1 details the synthesis procedure used for the preparation of 3D sponge-like carbons by using a simple and eco-friendly endo-templating or salt-templating approach. As carbon precursor, we have explored the use of a biomass derivative such as gluconic acid, which has a relatively high carbonization yield (20 wt%, see TGA analysis in Figure S1a) and melts at a low temperature of 131 °C, and as endo-template an abundant, economic, low toxicity and water-removable salt such as sodium carbonate (optimization of the Na_2CO_3/gluconic acid weight ratio was initially done as explained in the Supplementary Note 1). As will be shown, for $T \leq 600$ °C, Na_2CO_3 acts mainly as endo-template, whereas for higher temperatures, it has an additional role as activating agent. A freeze-drying approach was adopted to induce the self-assembly of the Na_2CO_3 particles into a 3D structure composed of roundish nanoparticles (which are covered by the carbon precursor) of around 90 to 260 nm (see Figure S2a). Since gluconic acid melts at relatively low temperatures, it flows in the first stage of the heat-treatment, ensuring the coverage of the Na_2CO_3 nanoparticles and the filling of interparticle voids, which leads to a carbon matrix embedding the Na_2CO_3 template nanoparticles (Figure S2b). The inorganic nanoparticles can be completely removed with water, as proved by the energy dispersive analysis in Figure S2c, yielding a material with a 3D sponge-like structure. As a control sample, gluconic acid was also directly carbonized at 600 °C, producing a glassy carbon made up of large bulky particles (Figure S3a). In addition, a sample was prepared by evaporating the water instead of freeze-drying, which led to a denser and heterogeneous structure (Figure S3b).

The chemical processes taking place when a mixture of gluconic acid and sodium carbonate is carbonized at high temperature under inert atmosphere were analyzed through thermogravimetric analysis (TGA) and temperature programmed desorption (TPD) experiments. For comparison, the same analyses were performed on pure gluconic acid. The corresponding TGA/DTG curves are depicted in Figures S1a and b, while the TPD profiles are shown in Figures S1c and d. As can be seen in Figure S1a, the decomposition of pure gluconic acid takes place in the range of ≈200 to 500 °C, with the most pronounced weight loss being recorded from 210 to 310 °C. That weight loss is mainly ascribed to the decarboxylation of gluconic acid, as inferred from the large CO_2 evolution in the corresponding TPD profiles (Figure S1c). When gluconic acid is mixed with sodium carbonate, the weight loss peaks corresponding to the decomposition of gluconic acid shift to temperatures below 200 °C (Figure S1b), with restricted evolution of CO_2 compared to pure gluconic acid (even if the dilution effect in the mixture is considered), as revealed by Figure S1d. Therefore, it seems that sodium carbonate inhibits the decarboxylation of gluconic acid, which was confirmed by FTIR analysis (see Figure S4 and related discussion). As will be shown later, this allows the final carbon material to retain a large oxygen content. In addition, Figure S1b shows a sharp weight loss above 600–700 °C and a slower rate weight loss for $T > 800$ °C. The first one leads to the evolution of CO (Figure S1d) and, accordingly, can be attributed to the redox reaction between carbon and Na_2CO_3 [Eq. (1)].[25]

$$Na_2CO_3 + 2\,C \rightarrow 2\,Na + 3\,CO \quad (1)$$

The second one is associated to a large CO_2 evolution and a minor CO evolution, as inferred from Figure S1d, and then may be ascribable to the following reactions [Eqs. (2) and (3)]:

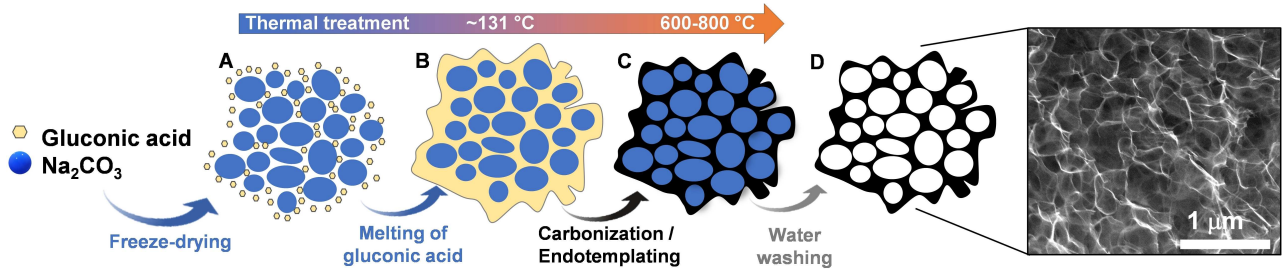

Scheme 1. Illustration of the salt-templating approach used for the production of the carbon anodes.

$$Na_2CO_3 \rightarrow Na_2O + CO_2 \quad (2)$$

$$CO_2 + C \rightarrow CO \quad (3)$$

The morphology of the carbon materials produced at different temperatures was examined by scanning electron microscopy (SEM). As shown by Figures 1a and b (600 °C) and S5a and b (a: 700 and b: 800 °C), regardless of the carbonization temperature, the materials display a sponge-like structure consisting of interconnected roundish cavities (which are the inverse replica of the Na_2CO_3 nanoparticles) of around 100 to 500 nm enclosed by very thin walls. Closer inspection by transmission electron microscopy (TEM) of AGNa-600 confirms the thinness of the sheets composing the walls of the nanocavities (Figure 1c). Further magnification by HRTEM reveals abundant microporosity within the walls, as well as the random distribution of domains of few graphene layers of small lateral size featuring an average interlayer spacing of ≈0.395 nm (inset in Figure 1d). This combination of porous thin walls providing short diffusional paths and a highly disordered microstructure with large interlayer spacing can greatly facilitate Na ion transport, as well as provide plenty of active sites for Na adsorption.

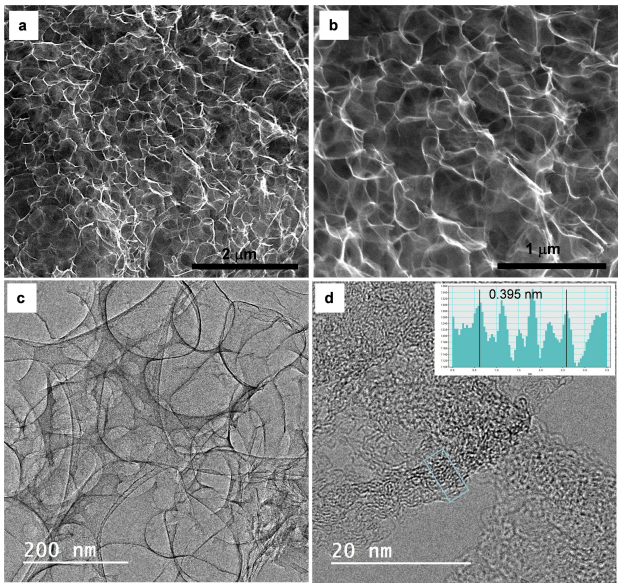

Figure 1. Micrographs of AGNa-600. a,b) SEM. c) TEM. d) HRTEM (with inset line scan spectrum).

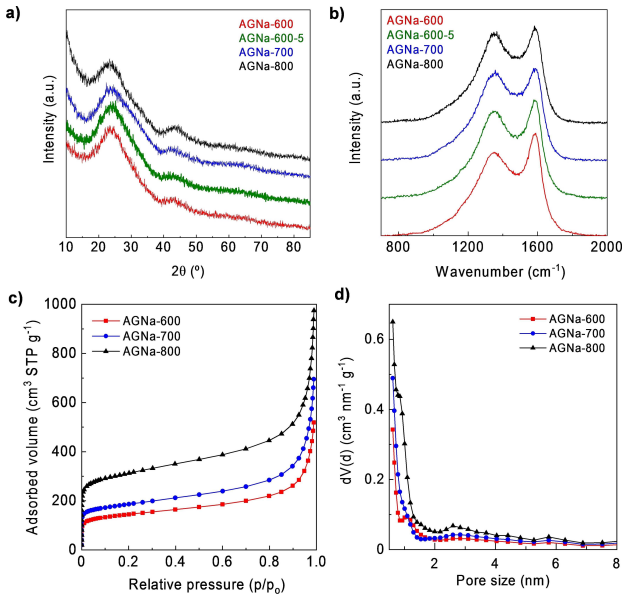

Figure 2. a) XRD diffractograms. b) First-order Raman spectra. c) N_2 adsorption isotherms. d) QSDFT pore size distributions of the carbon materials.

The microstructure of the materials was further characterized by X-ray diffraction and Raman spectroscopy. The diffractograms in Figure 2a are typical of highly disordered (turbostratic) carbons with domains composed of few graphene layers and with a small lateral size, as revealed by the broad and low intensity (002) and (10) diffraction bands. The average interlayer spacing calculated from the position of the (002) peak decreases with the increase of the synthesis temperature and the lengthening of the residence time, but all are considerably larger (9–11 %) than that of graphite (i.e., 0.335 nm) (Table 1). This large spacing guarantees the reversible insertion of Na ions.[26] The disordered microstructure is further corroborated by the Raman spectroscopy analysis. Thus, broad and overlapping D- and G-bands are identified in the first-order Raman spectra, as shown in Figure 2b. After deconvolution into four contributions (see Figure S6), integrated intensity ratios (I_D/I_G) in the 2.7–3 range are obtained. In the case of disordered carbons, the interpretation of the Raman spectra differs from that of graphitic carbons. Thus, as shown by Ferrari and Robertson, for small L_a, the D-mode strength is proportional to the probability of finding a six-fold ring in the cluster, that is, proportional to the cluster area.[27] These authors postulate that the development of a D peak in disordered carbons indicates ordering, exactly opposite from the case of graphite. Accordingly, the increase of (I_D/I_G) with the rise of temperature or extension of residence time indicates a higher ordering. This is further supported by the narrowing of the D- and G-bands (see Table 1).

The porous network of carbonized products was analyzed by N_2 physisorption at −196 °C. As shown in Figure 2c, the carbon materials obtained in the presence of Na_2CO_3 display a type I–IV isotherm with a pronounced capillary condensation step at relative pressures close to 1, which reveals that the porosity is made up of narrow micropores combined with large nanocavities (macropores) left by the removal of the Na_2CO_3 nanoparticles. In contrast, the material obtained by the carbonization of gluconic acid in the absence of Na_2CO_3 displays a type I isotherm (see Figure S7a) with a porosity almost exclusively formed by micropores (see Table 1). With the increase of the synthesis temperature, there is an increase in pore development and decrease of yield, which is the result of the redox reaction between carbon and Na_2CO_3, as determined in the TPD experiments (see above). Accordingly, Na_2CO_3 acts as

Table 1. Physico-chemical properties of the carbon materials.

Carbon material	Carbon Yield [%]	Textural properties				Structural properties				Chemical properties		Electronic conductivity [S cm^{-1}]
		S_{BET} [m^2 g^{-1}]	$V_{p0.99}$[a] [cm^3 g^{-1}]	$V_{p0.9}$[b] [cm^3 g^{-1}]	V_{micro}[c] [cm^3 g^{-1}]	d_{002} [nm]	I_D/I_G	FWHM [cm^{-1}]		C [wt%]	O[d] [wt%]	
								D	G			
AG–600	21	482	0.23	0.20	0.18	0.383	–	–	–	92.5	4.9	–
AGNa-600	23	533	0.80	0.40	0.18	0.375	2.67	261	98	86.5	12.2 (12.1)	0.08
AGNa-600-5	22	546	0.78	0.39	0.18	0.372	2.84	237	90	86.3	12.4 (12.5)	0.79
AGNa-700	22	690	1.08	0.53	0.23	0.364	2.93	236	95	90.9	8.7	2.5
AGNa-800	18	1160	1.51	0.79	0.40	0.367	2.97	236	90	93.0	6.2	5.7
Cathode material	20	2325	1.39	1.23	0.88	–	–	–	–	–	–	–

[a]. Pore volume determined at (P/P_0) = 0.99. [b]. Pore volume determined at (P/P_0) = 0.90. [c]. Volume of pores < 2 nm determined from the QSDFT PSD. [d]. The oxygen content determined through XPS is given in parenthesis.

activating agent, besides endo-template, for temperatures above 600 °C. This is specially marked at 800 °C, temperature at which the yield experiences a 22% decrease, and the BET surface area and micropore volume an approximately 120% increase, reaching values of 1160 m^2 g^{-1} and 0.40 cm^3 g^{-1} respectively (Table 1). The QSDFT pore size distributions in Figure 2d show that the pores confined within the nanocavity walls are in the micropore range for all the materials. On the other hand, we observed that the extension of the residence time at 600 °C hardly modifies the textural properties (Figure S7 and Table 1).

The chemical composition of the materials and the binding motifs of C and O atoms were analyzed by elemental chemical analysis and X-ray photoelectron spectroscopy (XPS), respectively. As listed in Table 1, the carbon materials obtained in the presence of Na_2CO_3 have a noticeable oxygen content, the amount decreasing with the increase of synthesis temperature from 12.2 wt% (600 °C) to 6.2 wt% (800 °C), but not with the extension of the residence time. By contrast, the carbon obtained by direct carbonization of gluconic acid has a much lower oxygen content of 4.9 wt% (600 °C). As inferred from the TPD and FTIR analyses, this is due to the inhibition of the decarboxylation of gluconic acid by Na_2CO_3. Therefore, this endo-template synthesis strategy with Na_2CO_3 has the additional benefit of allowing the incorporation of more oxygen groups into the carbon framework, which can contribute to enhancing the Na^+ storage capacity of the carbon material, as shown by previous studies.[28–30] The reduction in oxygen content with the rise of temperature, coupled with the certain improvement registered in microstructural ordering, translates into high electronic conductivities of approximately 3–6 S cm^{-1} at 700–800 °C. On the other hand, there is also an increment in the electronic conductivity of AGNa-600-5 even though the oxygen content is maintained (see Table 1), which can be explained by the better microstructural ordering measured by Raman spectroscopy. XPS analysis confirms the effectiveness of the water washing purification step (see survey spectra in Figures S8a and b). Moreover, the oxygen contents deduced by XPS match those obtained by elemental analysis (Table 1), which indicates a uniform distribution of the oxygen moieties throughout the particles. The high-resolution C 1 s and O 1 s XPS spectra obtained for the samples synthesized at 600 °C are shown in Figure S8c–f. Deconvolution of the high-resolution C 1s spectra reveals the presence of three different kinds of oxygen moieties: C–O (11.0–13.7%), C=O (5.4–5.8%) and O–C=O groups (5.1–5.5%). The quantitative analysis of the O 1 s high-resolution spectra reveals in both cases a large contribution of the peak ascribed to double-bonded oxygen to the overall signal (54–58%). This is worth highlighting since it has been reported that these functionalities can interact reversibly with sodium cations, and thus enhance the storage performance of the carbon. Comparison between the data obtained for AGNa-600 and AGNa-500-5 suggests that the extension of the residence time only brings about minute changes in oxygen speciation.

Electrochemical performance of the carbon materials as Na-ion anodes

The materials were analyzed in half-cells using Na foil as both counter-electrode and reference, and 1 M $NaClO_4$ in EC/DEC (1:1 vol.) as electrolyte. The Na storage capacity was first evaluated through galvanostatic charge/discharge experiments at increasing current rates from 0.1 to 10 A g^{-1} in the potential range of 0.01–3.0 V vs. Na/Na$^+$. Figure 3a shows the charge/discharge profiles at 0.1 A g^{-1} for the materials synthesized at different temperatures. With the increase in temperature, there is an increase in the irreversible loss of capacity during the first cycle, which yields a decreasing initial coulombic efficiency (ICE) from 49% at 600 °C to 24% at 800 °C. This can be ascribed to a larger irreversible loss of Na during the formation of the solid electrolyte interface (SEI), since it correlates with the specific surface area of the materials (see Table 1). On the other hand, the reversible capacity increases for lower synthesis temperature, with AGNa-600 and AGNa-700 exhibiting values of 307 and 304 mAh g^{-1} respectively (≈74 and 46 mAh cm^{-3} respectively), vs. 255 mAh g^{-1} (≈35 mAh cm^{-3}) for AGNa-800. As shown in Figure 3a, a good Na storage reversibility is obtained in all the cases with further cycling. All the profiles are essentially sloping, revealing a pseudocapacitive Na storage mechanism that includes Na^+ adsorption on the surface,

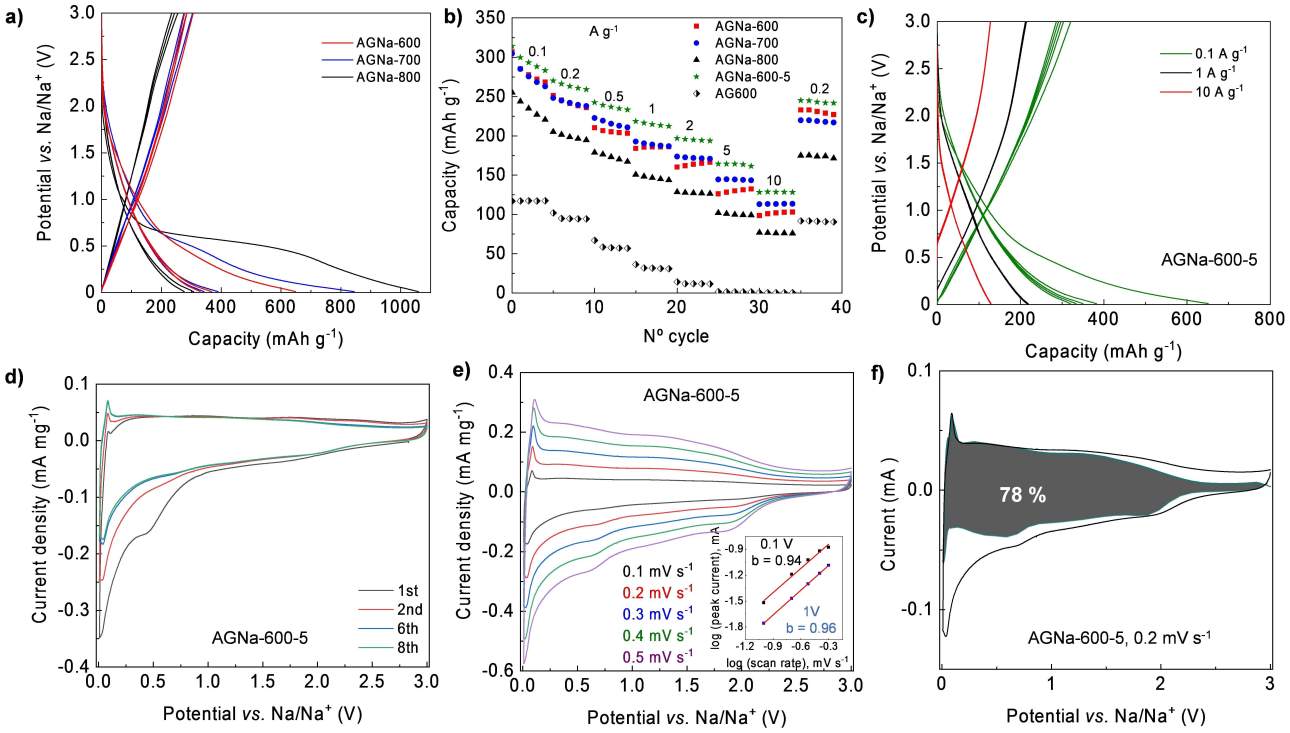

Figure 3. a) Three initial galvanostatic potential profiles at 0.1 A g^{-1}. b) C-rate capability of the carbon materials. c) Five initial potential profiles at different rates for AGNa-600-5. d) CVs at 0.1 mV s^{-1}. e) CVs at different scan rates for AGNa-600-5 (inset: plot of b-value). f) CV at 0.2 mV s^{-1}, including the pseudocapacitive contribution in dark grey.

oxygen functional groups, and defects (edge, vacancies, etc.).[31] Given that the samples obtained at lower temperatures have a less developed pore structure (see Table 1), the superior reversible capacity of AGNa-600 can be attributed to the high number of defective sites and O content. Indeed, oxygen groups containing C=O bonds can reversibly react with sodium ions through fast surface redox reactions.[6,28–30,32] This pseudocapacitive behavior coupled with the shortened diffusion pathways in the sponge-like structure (both within the liquid electrolyte and in solid-state in the thin walls) provides the materials with a good rate capability, as revealed by Figure 3b, with reversible capacities of 77–113 mAh g^{-1} at 10 A g^{-1} (which corresponds to a charge/discharge rate of 33 C, considering C = 300 mAh g^{-1}). On the contrary, even though the material obtained by the carbonization of gluconic acid alone at 600 °C exhibits also a pseudocapacitive behavior (see Figure S9), it provides a negligible capacity above 2 A g^{-1}, which reveals severe diffusion restrictions throughout its bulky structure, contrarily to the sponge-like materials. In addition, it exhibits also a low reversible capacity of 117 mAh g^{-1} at 0.1 A g^{-1}, which can be attributed to the lower oxygen content (Na uptake begins at much lower potentials, as revealed by Figure S9), besides the lower accessibility of the active sites. It should be noted that the rate capability of AGNa-700 is better than that of AGNa-600 owing to its much superior conductivity; however, this improvement takes place at the expense of a reduced ICE (i.e., 36%), which makes it unsuitable for Na storage. Importantly, Figure 3b shows that prolonging the residence time at 600 °C is the most effective strategy to optimize the performance of the material. Thus, AGNa-600-5 shows the highest reversible capacity regardless of the current density, with a value of 314 mAh g^{-1} at 0.1 A g^{-1} and ca. 130 mAh g^{-1} at 10 A g^{-1}. This improvement in rate capability can be ascribed to the 10-fold increased electronic conductivity (0.79 S cm^{-1} for AGNa-600-5 vs. 0.08 S cm^{-1} for AGNa-600–see Table 1), which reduces the charge transfer resistance, as evidenced by the smaller semicircle at high to medium frequencies in the Nyquist plot derived from EIS analysis (Figure S10 and Table S1), improving the utilization of the active sites. And this improvement of the rate performance does not occur at the expense of the ICE (see Figure 3c) since the textural properties of AGNa-600 and AGNa-600-5 are virtually the same. Overall, the capacity of the material in the carbonate electrolyte compares well with the state-of-the-art in surface-driven Na storage hard carbons (see Table S2).

From a practical viewpoint, it is worth mentioning that the ICE of AGNa-600-5 can be substantially improved from 49% up to 85% (value typical of low surface area hard carbons) by using an ether-based electrolyte (i.e., 1 M $NaPF_6$ in diglyme). Thus, as can be seen in Figure S11a, electrolyte decomposition during the first sodiation process is suppressed to a large extent, in agreement with previous studies.[33,34] Furthermore, the coulombic efficiency already reaches a value of 97% in the second cycle. Besides, an improved rate performance is recorded, with a capacity value as high as 174 mAh g^{-1} at 10 A g^{-1} (see Figure S11b), which can be attributed to the formation of a

thinner and more compact SEI layer, as shown in previous studies.[33–35] Finally, the cycling stability is also considerably improved in the ether electrolyte (Figure S11c), the capacity loss per cycle decreasing from 0.070 mAh g^{-1} in the carbonate electrolyte to 0.015 mAh g^{-1} in the ether electrolyte after 1400 cycles at 1 A g^{-1}. These results show that both rate capability and long-term stability could be enhanced by optimizing the electrolyte composition.

The sodium storage mechanism and its kinetics was further studied through CV experiments carried out at 0.1 mV s^{-1} for AGNa-600-5 (Figure 3d), AGNa-600 (Figure S12a) and AGNa-700 (Figure S12b) anodes. In all the cases, during the first sodiation there is an irreversible redox peak at approximately 0.5 V, especially pronounced in the case of AGNa-700 (Figure S12b), which disappears in the following cycles and corresponds to the electrolyte decomposition to yield the SEI layer, in agreement with the galvanostatic potential profiles in Figure 3a. Besides, the CVs display a quasi-rectangular shape for potentials $>$0.2 V vs. Na/Na$^+$, indicative of pseudocapacitive behavior, with broad bumps between 0.5 and 2.2 V vs. Na/Na$^+$ which could be ascribed to the interaction of Na$^+$ with defects and oxygen functional groups. In addition, a defined reversible redox peak is registered below 0.2 V, which would correspond to the Na$^+$ intercalation/de-intercalation between the graphene layers of the most ordered domains, but its contribution is minor, as inferred by its low intensity. With the increase of scan rate, the CVs retain the shape even for potentials below 0.2 V, suggesting that, unlike in ion intercalation processes, this redox process is not limited by diffusion (Figure 3e). A kinetic analysis was applied to the de-sodiation peak at approximately 0.1 V vs. Na/Na$^+$ and also at a potential of 1 V vs. Na/Na$^+$ by using the power law dependence of the peak current (i) on scan rate (υ) [Eq. (4)], wherein k and b are adjustable parameters.

$$i\,(V) = k\,\upsilon^{b} \tag{4}$$

The b value can be calculated by plotting log(i) vs. log(υ). A value of $b=0.5$ is indicative of a diffusion-controlled faradaic reaction, whereas $b=1$ indicates a surface capacitive/pseudocapacitive process.[36] The analysis produced values of $b=0.84$/0.84 for AGNa-600 (Figure S10c), $b=0.94$/0.94 for AGNa-700 (Figure S10d) and 0.94/0.96 AGNa-600-5 (Figure 3e), consistent both regions with a predominantly pseudocapacitive Na storage mechanism. To quantify the specific contributions of the capacitive and diffusion-control processes in the CVs, the Dunn's method was used to separate the total current (i) at a fixed potential (V) into two parts consisting of the capacitive current ($k_1\cdot\upsilon$) and diffusion-controlled current ($k_2\cdot\upsilon^{1/2}$) [Eq. (5)].[36]

$$i\,(V) = k_1\cdot\upsilon + k_2\cdot\upsilon^{1/2} \tag{5}$$

In this way, a pseudocapacitive contribution as large as 78% is already registered at 0.2 mV s^{-1}, as shown in Figure 3f.

Electrochemical performance of the Na-ion capacitor (NIC)

For the full NIC cell assembly, we used as cathode a highly porous carbon that was synthesized through a sustainable salt template-assisted chemical activation approach recently developed by our group. It is based on the use of KCl particles as template, and K_2CO_3 particles as both template and activating agent.[23,24] As can be seen in Figures S13a and b, the cathode material exhibits also a 3D sponge-like structure with thin interconnected carbon walls. However, in this case, the carbon walls possess plenty of micropores, as inferred from the N_2 adsorption isotherm in Figure S13c and the PSD in Figure S13d. Analysis of the N_2 adsorption data renders a BET surface area value of 2325 m^2 g^{-1}, with a micropore volume of 0.88 cm^3 g^{-1} and of 1.23 cm^3 g^{-1} for the total pore volume confined within the walls (Table 1). It is worth noting that the yield of the synthesis process, despite being an activation process based on carbon etching, is as high as 20% for this particular carbon precursor (compared to 14% for glucose or 10% for soybean meal).[23] It should be mentioned that, inspired by the anode synthesis process, a mixture of sodium carbonate and sodium chloride was also explored (using the same proportions as with the potassium salts), but led to a lower yield (16%) and poorer textural properties ($S_{BET}=1750$ m^2 g^{-1}, $V_{microp}=0.68$ cm^3 g^{-1} and of $V_p=1.06$ cm^3 g^{-1}), which may be ascribed to excessive carbon gasification (Figure S1d).

The cathode performance was assessed in the potential range of 2–4.2 V vs. Na/Na$^+$, which is the usual working potential range of carbon materials in the full cell device. Figure S14a shows almost linear potential profiles regardless of the current density evaluated, in accordance with a double-layer storage mechanism of ClO_4^- anions. As evidenced by Figure S14b, a reversible capacity of 95 mAh g^{-1} (38 mAh cm^{-3}) is achieved at 0.1 A g^{-1}, preserving still 52 mAh g^{-1} (21 mAh cm^{-3}) at 10 A g^{-1}, which supports its good rate capability.

Full NIC cells were assembled with the optimized anode material AGNa-600-5 and porous carbon described in the previous paragraph, analyzing the impact of two different mass balances (anode/cathode = 1:1 and 1:2) on the energy/power characteristics and the stability of the device. Before assembling the full cell, both the anode and cathode were pre-conditioned in half-cells. The full cell was measured within the voltage window of 1–4 V to avoid cation adsorption in the cathode. Figures 4a and b compare the galvanostatic charge/discharge voltage profiles of the NICs assembled with the different mass ratios at 1 and 10 A g^{-1} (calculated based on the mass of both electrodes). In both cases, symmetric linear profiles are registered regardless of the current rate, supporting the capacitive behavior of the hybrid device. The (1:2) NIC shows higher capacitance and capacity over the whole range of currents evaluated, with values of 52 F g^{-1} (45 mAh g^{-1}) at 0.1 A g^{-1} and 44 F g^{-1} (28 mAh g^{-1}) at 10 A g^{-1}, as can be seen in Figures 4c and d, owing to a better capacity balance between anode and cathode. In order to get further insights into the behavior of the anode and cathode during the operation of the full device for the different mass ratios, the performance of

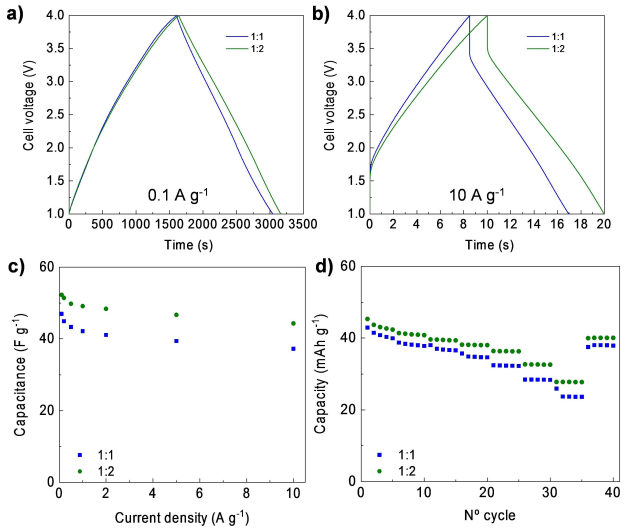

Figure 4. a,b) Electrochemical performance of the NICs assembled with different mass ratios: voltage profiles at 0.1 A g^{-1} or 10 A g^{-1}. c,d) Impact of the current rate on the capacitance and capacity.

each electrode was monitored by using a three-electrode cell equipped with a sodium reference electrode. Figures 5a and b show the corresponding potential profiles at 0.1 A g^{-1}, including the voltage profile of the NIC, while Figures 5c and d gather those at 10 A g^{-1}. With the increase of the ratio anode/cathode from 1:1 to 1:2, the potential swings of the anode and cathode become more similar due to their closer capacity values. As a result, there are slight decreases in the maximum and minimum potentials achieved respectively by the cathode and anode, which prevents the cathode from oxidation, but can cause sodium plating on the anode. This effect is even more marked at a high rate of 10 A g^{-1}, wherein the potential swing of the cathode decreases at the expense of the increase of the potential swing of the anode due to its smaller capacity compared to the cathode at high rates. Nevertheless, the minimum potential achieved by the anode is still 0.01 V vs. Na/Na^+ at 10 A g^{-1}. In spite of the deeper utilization of the anode in the (1:2) NIC, the rate performance is slightly improved, as shown by Figures 4c and d, which can be explained by the fast kinetics of its pseudocapacitive Na storage mechanism.

The long-term stability of the NICs was tested by galvanostatic charge/discharge cycling at 2 A g^{-1}. As revealed by Figure 6a, both NICs show a good capacity retention after 10000 cycles, with values of 69–71%. The slightly higher capacity fading of the (1:2) NIC suggests that the stability is more affected by the deeper use of the anode than the possible oxidation of the cathode. Figure 6b shows the energy-power characteristics of both NICs, highlighting the better behavior of the (1:2) NIC and its good performance compared to the state-of-the-art,[9,10,12,37–39] being able to store up to approximately 110 Wh kg^{-1} at low power and still 71 Wh kg^{-1} at approximately 26 kW kg^{-1}.

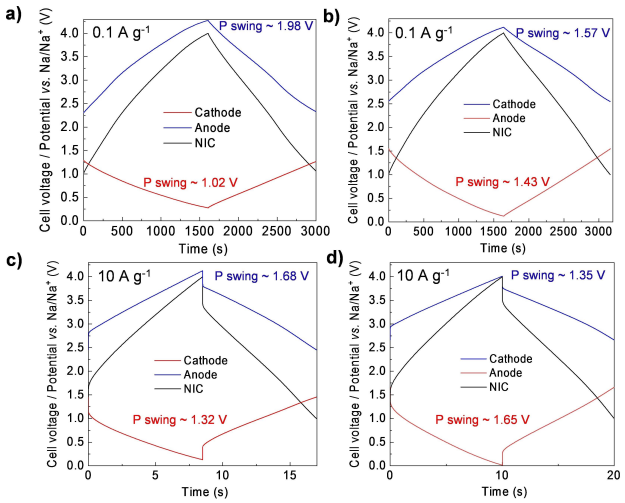

Figure 5. Galvanostatic potential profiles of the anode and cathode for the NICs assembled with different mass ratios. a,c) Potential profiles at 0.1 A g^{-1} or 10 A g^{-1} for a mass ratio of 1:1. b,d) Potential profiles at 0.1 A g^{-1} or 10 A g^{-1} for a mass ratio of 1:2.

Conclusions

A novel and sustainable approach was developed for the synthesis of a 3D sponge-like carbon exhibiting fast storage of Na ions. The approach followed a salt-templating strategy based on the use of gluconic acid as carbon precursor and a low-cost, low toxicity and water-removable salt such as sodium carbonate as endo-template. The optimized carbon material thus produced possessed a BET surface area of around 500 $m^2 g^{-1}$ with a 3D structure composed of thin interconnected carbon walls with a highly disordered microstructure. This kind of structure provided shortened diffusion distances to speed up sodium ions transport both within the liquid electrolyte and in the solid-state. Besides, in the presence of sodium carbonate, a high oxygen content of approximately 12 wt% was obtained compared to around 5 wt% for gluconic acid pyrolyzed in the absence of the salt at the same temperature. As a result, the material produced with the aid of the Na_2CO_3 as endo-template exhibited a high electrochemical performance based on a predominantly pseudocapacitive sodium storage mechanism,

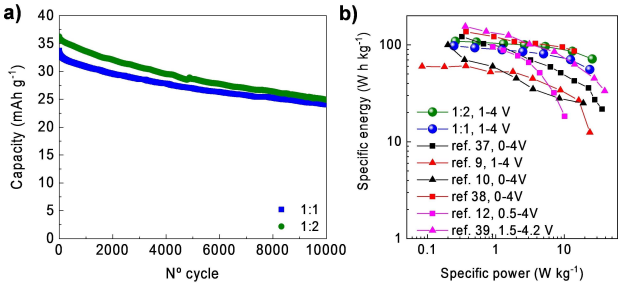

Figure 6. a) Long-term galvanostatic cycling at 2 A g^{-1} for the NIC devices. b) Ragone plot including a comparison to the state-of-the-art in NICs.

providing a capacity of 314 mAh g^{-1} at 0.1 A g^{-1} and still 130 mAh g^{-1} at 10 A g^{-1}.

Na-ion capacitors were assembled with a cathode consisting of a 3D highly porous carbon ($S_{BET} \approx 2300\ m^2 g^{-1}$) synthesized from the same precursor following a salt template-assisted chemical activation strategy based on the use of a mixture of K_2CO_3 and KCl. The NIC with an anode to cathode ratio of 1:2 provided remarkable energy-power characteristics in the voltage range of 1 to 4 V, as demonstrated by its capability to store up to ca. 110 Wh kg^{-1} at low power and up to 71 Wh kg^{-1} at ca. 26 kW kg^{-1}. Besides, it showed good long-term stability, retaining almost 70% of its capacity after 10000 cycles.

Experimental Section

Synthesis of anode carbon materials

Sodium carbonate (>99.5%, Sigma-Aldrich) was first dissolved in water, followed by the addition of D-(+)-Gluconic acid δ-lactone (GA) (Sigma-Aldrich), using a Na_2CO_3/GA weight ratio of 7:1. Afterward, the mixture was frozen in liquid nitrogen (-196 °C) and then transferred to a lyophilizer (Telstar Cryodos) and freeze-dried at a temperature of −50 °C and a pressure of 0.06 mbar. The solid thus obtained was heat-treated at temperatures in the range of 600–800 °C (3 °C min^{-1}) under nitrogen gas flow and held at the maximum temperature for 1 h (materials labeled AGNa-*T*, where *T* is the synthesis temperature). In addition, a sample was prepared by heat-treatment at 600 °C (3 °C min^{-1}) for 5 h (AGNa-600-5). The resulting carbon-Na_2CO_3 mixture was washed several times with hot distilled water to remove the Na_2CO_3 particles. Finally, the carbon product was dried in an oven at 120 °C for 3 h. For comparison, a sample of GA was also directly carbonized under N_2 at a temperature of 600 °C (3 °C min^{-1}, 1 h). This material was labeled AG600.

Synthesis of cathode carbon material

The cathode material was synthesized from GA following the procedure reported by our group.[23,24] Specifically, potassium chloride (>99.5%, Sigma Aldrich) was first dissolved in water, followed by the addition of potassium carbonate (Merck) and GA, using a K_2CO_3/KCl/GA weight ratio of 1:7:1. Afterward, the mixture was frozen in liquid nitrogen (-196 °C) and then freeze-dried. The solid thus obtained was heat-treated at a temperature of 850 °C (3 °C min^{-1}) under a nitrogen gas flow and held at the maximum temperature for 1 h. The resulting carbon-inorganic salts mixture was washed several times with hot distilled water to remove the inorganic salt particles and finally dried at 120 °C for several hours.

Physicochemical characterization

Scanning electron microscopy (SEM) images were acquired in a Quanta FEG650 (FEI) instrument, while high-resolution transmission electron microscopy (HRTEM) images were obtained on a JEOL (JEM 2100-F) apparatus operating at 200 kV. The N_2 sorption isotherms were measured at −196 °C using a Micromeritics ASAP 2020 sorptometer. The apparent surface area was calculated by applying the BET method, for which an appropriate relative pressure range was selected to ensure a positive line intersect of multipoint BET fitting (BET *C* constant > 0). The pore size distributions (PSD) were determined by using the Quench Solid State Density Functional Theory (QSDFT) method for nitrogen. X-ray diffraction (XRD) patterns were obtained on a Siemens D5000 instrument operating at 40 kV and 20 mA, using a Cu–Kα radiation source. Elemental analysis of the samples was carried out on a LECO CHN-932 microanalyzer and a LECO VTF-900 (oxygen content). The Raman spectra were recorded on a Horiba (LabRam HR-800) spectrometer. The source of radiation was a laser operating at a wavelength of 514 nm and a power of 25 mW. X-ray photoelectron spectroscopy (XPS) was carried out on a Specs spectrometer, using Mg–Kα (1253.6 eV) radiation from a double anode at 150 W. Thermogravimetric analysis (TGA) curves were recorded on a TA Instruments Q6000 TGA system. The electronic conductivity of the carbon powders was determined in a homemade apparatus in which the powders were placed between two plungers inside a hollow nylon cylinder (inner diameter of 8 mm) and then subjected to a pressure of 7.1 MPa. Equation (6) shows the formula used for the calculation of the conductivity, where *I* is the current (A), *h* is the height of sample inside the cylinder (cm), *A* is the cross section (cm^2) and *V* is the voltage drop (V).

$$\sigma = (I \cdot h)/(A \cdot V) \tag{6}$$

Electrochemical characterization

Both anode and cathode material slurries were prepared by mixing the active material with Super C65 carbon black and carboxymethyl cellulose (CMC) binder (M_W = 700 000, Sigma-Aldrich) in a wt% ratio of 80:10:10 and dispersed in water by magnetic stirring overnight. The slurry was then casted onto carbon-coated aluminum foil using the Doctor Blade technique, dried overnight at 105 °C under vacuum and finally subjected to calendering. Afterward, the coated foil was cut into discs with a diameter of 10 mm (active carbon mass loading ≈1 mg cm^{-2}). CR2032 coin-type cells were assembled in an Ar-filled glovebox using a Na metal disk (diameter = 12 mm) as counter and reference electrode, and a Whatman GF/C glass fiber disk as the separator (diameter = 16 mm). The electrolyte consisted of a solution of 1 M $NaClO_4$ in a mixture of carbonates (EC/DEC = 1:1 vol.). The electrochemical performance of the half-cells was tested at room temperature in a computer-controlled potentiostat (Biologic VMP3 multichannel generator). Galvanostatic charge/discharge (CD) experiments were recorded from 0.01 to 3.0 V vs. Na/Na^+ in the case of the anode material and from 2 to 4.2 V vs. Na/Na^+ in the case of the cathode material, using increasing current densities from 0.1 to 10 A g^{-1}. Cyclic voltammetry (CV) experiments were recorded for the anode material within the same potential window at sweep rates in the 0.1 to 0.5 mV s^{-1}. Electrochemical impedance spectroscopy (EIS) curves were obtained in the de-sodiated state after one discharge/charge cycle within a frequency range from 100 kHz to 1 mHz using an amplitude of 10 mV. The values of volumetric capacity/capacitance for the anode/cathode were calculated considering the packing density of the electrode and the mass fraction of active material, according to Fuertes et al.[40]

The NIC full cells were assembled using a three-electrode configuration (Swagelok T-cell) with a metallic Na reference electrode to record the changes in the electrode potentials of anode and cathode. The current collectors consisted of stainless-steel rods, the separator and electrolyte being the same as those in the half-cells. Before testing, the anode and cathode electrodes were pre-conditioned to compensate for the initial sodium losses. Thus, the AGNa-600-5 electrode was cycled three times between 0.01 and 3.0 V vs. Na/Na^+ at 0.1 A g^{-1}, setting a cut-off potential of 0.2 V vs. Na/Na^+. Meanwhile, the cathode was cycled three times between 2 and 4.2 V vs. Na/Na^+ at 0.1 A g^{-1}, setting a cut-off potential of 4.2 V vs. Na/Na^+. The weight ratio between the anode and cathode

active materials was set at 1:1 and 1:2 (keeping constant the total active mass in the device). The specific capacitance ($F\,g^{-1}$), specific energy ($Wh\,kg^{-1}$), and specific power ($W\,kg^{-1}$) of the device were calculated using the formulae [Eqs. (7)–(9)]:

$$C = \frac{I}{\left(\frac{dV}{dt}\right) \cdot M} \tag{7}$$

$$E = \frac{1}{2} \cdot C \cdot (V_{max}^2 - V_{min}^2) \tag{8}$$

$$P = \frac{E}{\Delta t_d} \tag{9}$$

where I is the current, M is the total mass of active materials in the cathode and anode, dV/dt = slope of the discharge curve, ΔV_d is the operation voltage (V_{max}-IR_{drop}-V_{min}) and Δt_d is the discharge time.

Acknowledgements

This research work was supported by project IDI/2018/000148 (FICYT/FEDER) and PID2021-123648OB–I00 (MCIN/AEI/10.13039/501100011033/and ERDF A way of making Europe).

Conflict of Interest

The authors declare no conflict of interest.

Data Availability Statement

Research data are not shared.

Keywords: carbon · energy storage · hybrid ion capacitor · porous carbon · sodium

[1] K. Nobuhara, H. Nakayama, M. Nose, S. Nakanishi, H. Iba, *J. Power Sources* **2013**, *243*, 585–587.
[2] H. Yamamoto, S. Muratsubaki, K. Kubota, M. Fukunishi, H. Watanabe, J. Kim, S. Komaba, *J. Mater. Chem. A* **2018**, *6*, 16844–16848.
[3] A. Kamiyama, K. Kubota, D. Igarashi, Y. Youn, Y. Tateyama, H. Ando, K. Gotoh, S. Komaba, *Angew. Chem. Int. Ed.* **2021**, *60*, 5114–5120; *Angew. Chem.* **2021**, *133*, 5174–5180.
[4] A. Kamiyama, K. Kubota, T. Nakano, S. Fujimura, S. Shiraishi, H. Tsukada, S. Komaba, *ACS Appl. Energ. Mater.* **2020**, *3*, 135–140.
[5] Q. Meng, Y. Lu, F. Ding, Q. Zhang, L. Chen, Y.-S. Hu, *ACS Energy Lett.* **2019**, *4*, 2608–2612.
[6] W. Chen, C. Chen, X. Xiong, P. Hu, Z. Hao, Y. Huang, *Adv. Sci.* **2017**, *4*, 1600500.
[7] G. Wang, M. Shao, H. Ding, Y. Qi, J. Lian, S. Li, J. Qiu, H. Li, F. Huo, *Angew. Chem. Int. Ed.* **2019**, *58*, 13584–13589; *Angew. Chem.* **2019**, *131*, 13718–13723.
[8] J. Ding, Z. Li, K. Cui, S. Boyer, D. Karpuzov, D. Mitlin, *Nano Energy* **2016**, *23*, 129–137.
[9] R. Yan, K. Leus, J. P. Hofmann, M. Antonietti, M. Oschatz, *Nano Energy* **2020**, *67*, 104240.
[10] Q. Yu, T. Dong, R. Qiu, H. Wang, *Mater. Res. Bull.* **2021**, *138*, 111211.
[11] J. Ding, H. Wang, Z. Li, K. Cui, D. Karpuzov, X. Tan, A. Kohandehghan, D. Mitlin, *Energy Environ. Sci.* **2015**, *8*, 941–955.
[12] R. Yan, E. Josef, H. Huang, K. Leus, M. Niederberger, J. P. Hofmann, R. Walczak, M. Antonietti, M. Oschatz, *Adv. Funct. Mater.* **2019**, *29*, 1902858.
[13] L. Zhang, J. Sun, H. Zhao, Y. Sun, L. Dai, F. Yao, Y. Fu, J. Zhu, *J. Power Sources* **2020**, *475*, 228679.
[14] P. Lu, Y. Sun, H. Xiang, X. Liang, Y. Yu, *Adv. Energy Mater.* **2018**, *8*, 1702434.
[15] B. Cao, H. Liu, B. Xu, Y. Lei, X. Chen, H. Song, *J. Mater. Chem. A* **2016**, *4*, 6472–6478.
[16] Y. Wang, Y. Wang, J. Liu, L. Pan, W. Tian, M. Wu, J. Qiu, *Carbon* **2017**, *122*, 344–351.
[17] S. Zhu, J. Li, C. He, N. Zhao, E. Liu, C. Shi, M. Zhang, *J. Mater. Chem. A* **2015**, *3*, 22266–22273.
[18] S. Zhu, J. Li, L. Ma, L. Guo, Q. Li, C. He, E. Liu, F. He, C. Shi, N. Zhao, *ACS Appl. Mater. Interfaces* **2016**, *8*, 11720–11728.
[19] B. Liu, M. Yang, H. Chen, Y. Liu, D. Yang, H. Li, *J. Power Sources* **2018**, *397*, 1–10.
[20] D. Wang, Z. Wang, Y. Li, K. Dong, J. Shao, S. Luo, Y. Liu, X. Qi, *Appl. Surf. Sci.* **2019**, *464*, 422–428.
[21] Z. Wang, X. Wang, Y. Bai, H. Yang, Y. Li, S. Guo, G. Chen, Y. Li, H. Xu, C. Wu, *ACS Appl. Mater. Interfaces* **2020**, *12*, 2481–2489.
[22] L. Zou, Y. Lai, H. Hu, M. Wang, K. Zhang, P. Zhang, J. Fang, J. Li, *Chem. Eur. J.* **2017**, *23*, 14261–14266.
[23] N. Diez, G. A. Ferrero, A. B. Fuertes, M. Sevilla, *Batteries & Supercaps* **2019**, *2*, 701–711.
[24] N. Diez, G. A. Ferrero, M. Sevilla, A. B. Fuertes, *J. Mater. Chem. A* **2019**, *7*, 14280–14290.
[25] J.-W. Kim, H.-G. Lee, *Metall. Mater. Trans. B* **2001**, *32B*, 17–24.
[26] Y. Cao, L. Xiao, M. L. Sushko, W. Wang, B. Schwenzer, J. Xiao, Z. Nie, L. V. Saraf, Z. Yang, J. Liu, *Nano Lett.* **2012**, *12*, 3783–3787.
[27] A. C. Ferrari, J. Robertson, *Phys. Rev. B* **2000**, *61*, 14095–14107.
[28] Y. Shao, J. Xiao, W. Wang, M. Engelhard, X. Chen, Z. Nie, M. Gu, L. V. Saraf, G. Exarhos, J.-G. Zhang, J. Liu, *Nano Lett.* **2013**, *13*, 3909–3914.
[29] H. Zhao, J. Ye, W. Song, D. Zhao, M. Kang, H. Shen, Z. Li, *ACS Appl. Mater. Interfaces* **2020**, *12*, 6991–7000.
[30] F. Sun, H. Wang, Z. Qu, K. Wang, L. Wang, J. Gao, J. Gao, S. Liu, Y. Lu, *Adv. Energy Mater.* **2021**, *11*, 2002981.
[31] Y. Li, Y.-S. Hu, M.-M. Titirici, L. Chen, X. Huang, *Adv. Energy Mater.* **2016**, *6*, 1600659.
[32] L. Chen, L. Bai, J. Yeo, T. Wei, W. Chen, Z. Fan, *ACS Appl. Mater. Interfaces* **2020**, *12*, 27499–27507.
[33] Y. Zhen, R. Sa, K. Zhou, L. Ding, Y. Chen, S. Mathur, Z. Hong, *Nano Energy* **2020**, *74*, 104895.
[34] J. Pan, Y. Sun, Y. Yan, L. Feng, Y. Zhang, A. Lin, F. Huang, J. Yang, *JACS* **2021**, *1*, 1208–1216.
[35] J. Zhang, D.-W. Wang, W. Lv, S. Zhang, Q. Liang, D. Zheng, F. Kang, Q.-H. Yang, *Energy Environ. Sci.* **2017**, *10*, 370–376.
[36] J. Wang, J. Polleux, J. Lim, B. Dunn, *J. Phys. Chem. C* **2007**, *111*, 14925–14931.
[37] G. Dong, H. Wang, W. Liu, J. Shi, S. Sun, D. Li, H. Zhang, Y. Yang, Y. Cui, *ACS Appl. Energ. Mater.* **2018**, *1*, 5636–5645.
[38] L. Liu, X. Sun, Y. Dong, D. Wang, Z. Wang, Z. Jiang, A. Li, X. Chen, H. Song, *J. Power Sources* **2021**, *506*, 230170.
[39] H. Liu, X. Liu, H. Wang, Y. Zheng, H. Zhang, J. Shi, W. Liu, M. Huang, J. Kan, X. Zhao, D. Li, *ACS Sustainable Chem. Eng.* **2019**, *7*, 12188–12199.
[40] A. B. Fuertes, G. A. Ferrero, M. Sevilla, *Energy Storage Mater.* **2016**, *4*, 154–155.

Manuscript received: June 1, 2022
Revised manuscript received: July 14, 2022
Accepted manuscript online: July 26, 2022
Version of record online: August 16, 2022